Use of high-refractive index hydrogels and tissue clearing for large biological sample imaging

Alexander Richardson[1,a], Sandra Fok[2,a], Victoria Lee[1], Kerry-Anne Rye[1], Nick Di Girolamo[1], Blake J. Cochran[1]*

[1]School of Medical Sciences, UNSW Sydney, Sydney, NSW 2052, Australia

[2]Biomedical Imaging Facility, Mark Wainwright Analytical Centre, UNSW Sydney, Sydney, NSW 2052, Australia

[a]These authors contributed equally

*Corresponding author:

Blake J Cochran

School of Medical Sciences

UNSW Sydney

NSW 2052 Australia

b.cochran@unsw.edu.au

ABSTRACT

Recent advances in tissue clearing and light sheet fluorescence microscopy have allowed for improved insights and understanding of tissue morphology and disease pathology by imaging large samples without the requirement of histological sectioning. However, sample handling and ensuring sample integrity during lengthy staining and acquisition protocols remains a challenge. This study describes the use of acrylamide hydrogels synthesised to match the refractive index of solutions typically utilised in aqueous tissue clearing protocols. These hydrogels have a high water content (82.0±3.7% by weight). The gels remained stable over time and FITC-IgG was readily able to permeate into them, and efflux out of them. Whilst gels deformed and/or swelled over time in some commonly used solutions, this was overcome by using a previously described custom RIMS solution. To validate their use, CUBIC cleared mouse tissues and whole embryos were embedded in hydrogels, stained using fluorescent small molecule dyes, labels and antibodies and successfully imaged using light sheet fluorescence microscopy. The high water content, high refractive index hydrogels described in this study have a broad applicability to research that delves into pathophysiological processes via the stabilisation and protection of large and fragile samples.

INTRODUCTION

The use of histological approaches to understand physiology and pathology have traditionally relied on the use of optical imaging modalities. However, the opaque nature of many biological samples is a major limitation to this approach. To an extent, serial sectioning can be used to overcome this, with light scattering significantly decreased when tissues are sectioned into slices generally less than 100 μm thick. A major drawback to this approach is that the original 3-dimensional tissue architecture is not preserved. Whilst algorithms that automatically align serial sections can be utilised, sectioning of tissue always leads to non-linear tissue distortion. The advent of tissue clearing and whole-mount imaging systems such as light sheet fluorescence microscopy (LSFM) effectively overcomes this limitation, facilitating the visualistion of cell-to-cell interactions within complex 3-dimensional tissue architectures.

Tissue clearing techniques achieve transparency via removal of lipids and/or increasing the refractive index of the tissue. Tissue clearing techniques that effectively reduce light scattering[1,2] include aqueous-based methods such as CLARITY[3,4], CUBIC[5-7], TDE[8], SeeDB[9], SCALE[10] and MYOCLEAR[11] and organic solvent based-clearing such as BABB[12], DISCO[13,14] and PEGASOS[15]. Combined with LSFM, an unobstructed view of a whole intact tissue can be obtained[16]. The use of tissue clearing and LSFM has grown substantially in recent years and is now a widely utilised research tool in the biomedical sciences. Despite these advances, a number of challenges remain.

One major impediment is that tissues can undergo multiple rounds of expansion and/or shrinkage during the clearing process. However, these changes in tissue size do not result in tissue disruption in the final cleared product and have a minimal impact on outcomes[3,14,17]. In fact, increasing tissue volume can be used to increase resolution[18,19], whereas decreasing the volume can be advantageous for large samples[20-22]. Beyond the impact of clearing protocols on

tissue size, the chosen method can alter the mechanical properties of the sample. For example, SCALE creates cleared tissues that are too fragile to handle[1], SHIELD produces a sturdy tissue that can undergo multiple rounds of antibody labelling[23] and AdvCUBIC creates tissues with mechanical properties very similar to uncleared tissue[24]. DISCO, on the other hand yields a hardened, yet transparent tissue with very similar refractive index to glass[25]. Furthermore, the transparency of organic solvent-based cleared samples diminishes with long-term storage as exposure to oxygen induces crystallization. Encasement of DISCO cleared tissue in refractive index matched resin can prevent crystallisation, preserve fluorescence and improved sample handling and long-term storage[26].

Herein, we generated hydrogels with a refractive index that matches the CUBIC tissue clearing solutions[27]. The synthesized hydrogel can be used to improve sample stability and handling of cleared tissues. Our findings show fluorescence-conjugated antibodies can freely diffuse in and out of these gels, allowing for efficient staining of samples. Finally, we demonstrate that large biological samples including mouse embryos and whole organs can be embedded in hydrogel, stained, and imaged successfully imaged by LSFM. This work has broad applicability to both physiological and pathological research at the whole-organ level in humans and model organisms and has the added the advantage of stabilizing and protecting samples.

RESULTS

Synthesis of high refractive index hydrogels

Hydrogels composed of acrylamide (Figure 1A), methacrylamide (Figure 1B) and TEDA (Figure 1C) [27] were synthesized and evaluated for size changes (Figure 1D) and water content (Figure 1E). When immersed in distilled water, the hydrogels swelled significantly after 5 h ($p<0.01$), 15 h ($p<0.005$) and 24 h ($p<0.05$) (Figure 1D). This is consistent with uptake of water into the gel. Subsequent analysis found that the water content of the equilibrated gels was 82.0 ± 3.7% (Figure 1D), similar to previous investigations[27].

Antibodies penetrate high refractive index hydrogels and gels remain stable over time

To determine whether hydrogels were permeable to fluorescently labelled antibodies, gels were immersed in a solution of IgG-FITC for 7 days (Figure 2A). The gels gained green fluorescence over 6 days h, which was maximal at 567.8 ± 74.34% above baseline at 5 days ($p<0.0001$) (Figure 2A). A second group of gels were immersed in IgG-FITC solution for 6 days, then washed in TBS-T to determine if IgG-FITC could elute from the gel (Figure 2B). Green fluorescence was lost in a time-dependent manner, reaching 7.74 ± 4.1% of what was observed prior to the first wash (Figure 2B) ($p<0.0001$).

It was also necessary to determine if the structure of the gel was fixed following cross-linking. Therefore, gels were synthesized with microbeads that fluoresce when excited by a 488 nm wavelength and bead movement was measured over time (Figure 2C). When gels were imaged over 100 s, an r-squared coefficient of 0.737 was found when images were overlayed. This is indicates that there is a high degree of overlap between the initial and final time-points, and is consistent with minimal structural motility within the gel.

This data demonstrates that fluorescently labelled antibodies penetrate and are eluted from our high refractive index hydrogels without non-specific binding, indicating that they are amenable to immune-labelling of embedded tissues. Furthermore, as the gels are inherently stable over time, embedded tissues will remain in a stable configuration, which enables repeat imaging.

Hydrogels change size and shape in different refractive index (RI) solutions

As tissues shrink and expand in CUBIC solutions, it was important to establish how the gels react to different solutions prior to embedding optically cleared tissue in the hydrogels[6]. We synthesized 1 cm^3 hydrogels and immersed them in distilled water, CUBIC 1, CUBIC 2 or RIMS for up to 7 days (Figure 2D) and tracked changes in size over time. Hydrogels that were immersed in water swelled significantly at all time points ($p<0.05$) (Figure 1E). Maximal swelling was reached at 8 h (112.6±4.7% vs 0 h) (Figure 2E). When immersed in CUBIC 1, a small, but significant (92.4±4.7%; $p<0.05$ vs 0 h) decrease in gel size was noted at 8 h (Figure 2F). However, by 7 days the gel had swelled significantly (118.8±7.5% vs 0 h; $p<0.0001$) (Figure 2F). While hydrogels that were placed in CUBIC 2 had significantly decreased in size at 4 h (89.0±6.8% vs 0 h; $p<0.01$), 8 h (89.6±5.3% vs 0 h; $p<0.01$) and 24 h (91.9±2.5% vs 0 h; $p<0.05$), they had returned to the original size by 7 days (100.9±8.2% vs 0 h) (Figure 2G). However, these gels cracked, which could lead to impairment in image acquisition. As gels that were immersed in RIMS did not change in size or fracture over 7 days (Figure 2H), this solution was chosen as the imaging media for subsequent studies.

Stable imaging and 3D reconstruction of optically cleared, whole-mount mouse organs

Proof-of-concept imaging was performed during which we embedded cleared mouse tissues (Figure 3A and 3B) in hydrogels, immuno-stained them with Hoechst 33342 nuclear stain, anti-αSMA, and lectin, then acquired fluorescent images using LSFM (Figures 3 and 4). This combination of stains includes a nuclear dye (Hoechst 33342), an antibody against αSMA that

detects blood vessels and lectin, a general dye that binds to glycoproteins. Using these reagents, we accurately reconstruct whole-mount E12.5 embryos and identified various anatomical features such as the paws, tail, sinuses, vessels, and some internal organs such as the highly vascularized liver (Figure 3C-3E). A high degree of co-localization was observed between lectin (red) and αSMA (green) (Figure 3E). Older embryos (E14.5) were also stained for lectin and αSMA and the whole sample was rendered following image acquisition (Figure 3F and Movie S1). A high degree of detail became visible, including the developing cranial and ocular blood supply, as well as in the limbs and internal organs such as the liver (Figure 3F and Movie S1). When only the head was examined, it was apparent that lectin (red) bound to the sinus cavities, while αSMA expression was localised to numerous blood vessels throughout the head and facial region (Figure 3G-3I).

Further imaging was also performed on cleared heart (Figure 4A-4F) and kidney (Figure 4G-4I) samples. An accurate reconstruction of the vasculature, including the aorta and vena cava was generated when the tissue was stained with Hoechst (Figure 4A-4C). Moreover, the auricles, together with their blood supply were visible when the tissue was stained with both lectin and αSMA (Figure 4D-4F). Whilst a whole adult mouse kidney was too large to be imaged as a whole tissue, certain anatomical features were visualised including the ureteric artery (Figure 4G), nephron loops (Figure 4H, closed arrows) and internal vasculature (Figure 4H, open arrows) which could be rendered using a volumetric segmentation (Figure 4I). Overall, these results demonstrate the viability and applicability of utilising large, hydrogel-embedded biological samples for investigations into a wide variety of research areas including development, and physiological and pathological scenarios.

DISCUSSION

Hydrogels are defined as a gel containing water in a three-dimensional cross-linked polymeric network formed with one or more monomers. Based on environmental changes, hydrogels can absorb or release fluids. The ability to synthesise hydrogels with tuneable physical and chemical characteristics makes them a favourable material for use in tissue engineering, ophthalmology, wound dressing and various other biomedical applications[29]. Herein, we evaluated the applicability of a high RI hydrogel that provided stability to tissue architecture and minimised shrinking/expanding of the tissue for use in imaging large biological samples [6,17]. Typically, hydrogels have either a high RI or high water content, but not both. A high water content in hydrogels allows for efficient diffusion of drugs, peptides, proteins, oxygen and metabolites, whereas a high RI is desired for imaging where matching of the RI of amino acids and proteins (1.53-1.54) is important[30]. When the RI of tissue, surrounding fluid and hydrogel are matched, Snell's law applies where the speed of light does not change when entering different media, resulting in no reflection and refraction, thereby rendering the whole unit transparent. The hydrogel utilised in this study has both a high RI and high water content, resulting in an ideal material for use in both imaging and diffusion studies[27].

Movement or retardation of proteins throughout the porous network of a hydrogel is determined by several factors including electrostatic force, hydrophobic interactions, temperature and pH[31]. In this study, FITC-labelled IgG (~13 nm diameter) was found to efficiently diffuse into and out of the hydrogel. This compatibility of the hydrogel with antibodies is important for the detection of specific cell or tissue types by immunolabelling, which together with tissue clearing can render visible the internal structures of large biological samples.

Tissue clearing combined with LSFM allows for the visualisation of intact biological tissues without the requirement of tissue sectioning[32]. One important consideration when conducting

LSFM is sample mounting, with agarose and phytagel being commonly used. However, samples are typically limited to less than 3 mm due to image distortion caused by refractive index mismatching between the gel scaffold and imaging media. Glues, hooks and customised holders are routinely used to mount whole, large samples such as mouse brains, but this can damage the sample. Glues can also cause light scattering where the tissue is in contact with the adhesive. To date, only a limited number of studies have investigated the utility of alternative methods of sample mounting for LSFM imaging of large biological samples. High RI resin has been used to match the RI and protect samples that have been cleared with organic solvent from oxidation, handling and preservation of GFP fluorescence in mouse brains[26]. Low cost polydimethylsiloxane cuvettes with comparable optical properties to quartz have also been used to mount whole mouse brains for LSFM[33]. We have improved on these approaches by utilising a high RI hydrogel for sample stabilisation over long periods, enabling immuno-staining of large samples and repeated staining of the same sample without compromising tissue architecture. We also found that the improved structural integrity of samples embedded in the high RI hydrogel decreased the likelihood of structural deformation due to external movement of the sample holder through the viscous imaging media. This resulted in improved tiling, stitching and co-registration of samples that required multiple acquisitions.

While this method has been validated on intact mouse embryos and portions of both heart and kidney, the limiting factor in our ability to image larger samples was the resident microscope, with a small imaging chamber and limited X, Y, Z movement. However, with the appropriate hardware, the method of maintaining tissue architecture using high water content, high RI hydrogels as described here, will allow image acquisition of even the largest samples, including those from humans[34]. This method is applicable for researchers studying a multitude of fields and could be of use for especially large or fragile samples such as whole brains or vasculature, or to perform repeat staining of fresh or stored samples for follow up imaging, such as clinical

pathology samples[17]. Whilst this research used the CUBIC tissue clearing system, it is likely that this protocol would also be suitable for use with other tissue clearing protocols.

METHODS

Hydrogel synthesis

High RI hydrogels were synthesized as previously described[27]. In brief, acrylamide (Sigma-Aldrich) and methacrylamide monomers (Sigma-Aldrich) (3:7 ratio) were prepared in MilliQ water and cross-linked with 9% (w/v) tri(ethylene glycol) dimethylacrylate (TEDA) (Sigma-Aldrich). The solution was heated to 60ºC for 20 min to completely dissolve the monomers, then cooled to room temperature (RT), followed by the addition of 2,2'-azobis[2-(2-imidazolin-2-yl)propane] dihydrochloride (0.05% (w/v)) (Wako Chemicals), a temperature-dependent cross-linking initiator. The solution was poured into polydimethylsiloxane (PDMS) moulds, and a thin layer of mineral oil (Singer) was applied to create an anoxic environment prior to incubation at 37 ºC for 1 h. The polymerized gels were removed from the moulds and immersed in PBS for 2 days, with at least 2 changes of PBS to remove non-crosslinked monomers.

Water content

Water content of hydrogels was measured as previously described[27]. In brief, samples (n=8) were immersed in distilled water and equilibrated for ~2 days, then weighed on a 5-point analytical balance. The gels were then freeze-dried and weighed again. Water content was determined using the following formula:

$$\text{Water content (\%)} = \frac{\text{mass}_{\text{hydrogel}} - \text{mass}_{\text{dry}}}{\text{mass}_{\text{hydrogel}}} \times 100$$

Antibody penetration

Hydrogels (n=6/time point) were immersed in a solution of fluorescein-conjugated human IgG (IgG-FITC, final concentration 1 mg/mL) (Sigma-Aldrich) in TBS containing 0.1% (v/v) Triton X-100 (TBS-T). Antibody penetration was observed from wide-field fluorescence images (excitation 470/22 nm, emission 510/42 nm) that were obtained at 24 h intervals over 6 days. Antibody diffusion out of the gel was evaluated in a second set of gels (n=6/time point)

that had been immersed in IgG-FITC for 6 days. The gels were then washed in TBS-T, which was changed daily and images were acquired using wide-field fluorescence (excitation 470/22 nm, emission 510/42 nm). All gels were bisected prior to imaging to facilitate visualization of the central region. Fluorescence intensity was analyzed at three regions within the centre of the gel using ImageJ software (NIH, https://imagej.nih.gov/ij/download.html).

Gel motility

Gel motility and stability was assessed by the movement of fluorescent beads over time. Hydrogels were synthesized as described above with the addition of microbeads (50 nm diameter, Thermo Fisher) that fluoresce when excited at 488 nm. Bead-containing gels were analyzed by LSFM every 10 s for 100 s, and images at t=0 and t=100 s were compared by co-localization in ImageJ software (NIH).

Hydrogel size change in different RI-matched solutions

Prior to selecting a RI-matched solution for imaging, we determined how the hydrogels react to immersion in distilled water, CUBIC solutions 1 and 2[6], and a custom RI-matched solution (RIMS)[28]. CUBIC-1 comprising 25% (w/w) quadrol ((Ethylenedinitrilo) tetra-2-propanol) (Sigma-Aldrich), 25% (w/w) urea (Sigma), and 35% (w/w) dH_2O was stirred on a heat block set to 50 ^oC until all components were completely dissolved. Triton X-100 (15% (w/w, Sigma-Aldrich) was added and the solution was stirred at room temperature until optically clear. CUBIC-2 was prepared by mixing 50% (w/w) sucrose, 25% (w/w) urea and 15% (w/w) MilliQ water together, stirring at 80 ^oC on a heat block until dissolved then cooling to room temperature. Triethanolamine (10% (w/w), Sigma-Aldrich) was added, and the solution mixed at room temperature. RIMS was prepared with 32.4% (w/v) 60% Iodixanol (OptiPrep, Sigma-Aldrich), 29.4% (w/v) diatrizoic acid (Sigma-Aldrich) and 23.5% (w/v) N-methyl-d-glucamine (Sigma-Aldrich) in MilliQ water. Images were acquired following immersion of the samples

in the hydrogel for 7 days, and analysed using ImageJ software. The results are expressed as a % size change relative to T=0 h.

Animals

All animal procedures were conducted in accordance with the UNSW Sydney Animal Care and Ethics Committee guidelines (ACEC 17/81A). Male and female C57BL/6 mice between 6-8 weeks of age were studied. Embryos were generated by timed-mating as previously described [2]. Briefly, female mice were scented for 3 days (i.e. placed in a cage that previously housed male mice) prior to being placed with a male. The next morning the female mice were checked for the presence of a vaginal plug, which signified embryonic day (E) 0.5. All mice were euthanized by cervical dislocation following immersion in an isoflurane vaporizer. Tissues and embryos were dissected and fixed in 4% (v/v) paraformaldehyde (Sigma-Aldrich) overnight at 4 ºC, then washed in PBS and stored at 4 ºC.

Tissue clearing

Tissues, including heart and kidney, and E12.5 and E14.5 embryos were optically cleared using the CUBIC protocol as previously described[6]. In brief, tissue was immersed in CUBIC 1 solution, which was changed every 2-3 days until the sample was visibly clear (Figure 3A and 3B). The samples were then washed in PBS for 3 days with at least 3 changes of solution prior to further use.

Embedding cleared tissue in hydrogel and immunostaining

Cleared tissues were immersed in hydrogel solution and allowed to equilibrate for 48 h, then cross-linked as described above. The samples were washed over 24 h with at least 3 changes of PBS, then immunofluorescently stained using Hoechst 33342 nuclear stain, an anti-alpha-smooth muscle actin (αSMA) antibody conjugated to AlexaFluor-488 (Abcam), and lectin conjugated to DyLight-649 (Vector Labs) in TBS-T containing 2% (w/v) bovine serum albumin (TBS-T/BSA) for 7 days at 4 ºC. The samples were then washed in TBS-T/BSA for a

further 3 days, with at least 3 changes of the buffer. Finally, the samples were immersed in RIMS to ensure the correct RI for image acquisition.

Light sheet fluorescence microscopy (LSFM)

Images of immunostained samples were acquired by LSFM using the following settings: Hoechst 33342: excitation 458 nm, emission band pass 460-500 nm; Alexafluor 488: excitation 488 nm, emission band pass 505-545 nm; DyLight 649: excitation 638 nm, emission long pass 600 nm. A tiled series of z-stacks between 800-1000 images with 10% overlap were acquired and processed with Vision 4D (Arivis) software.

Statistical analysis

Results were analysed for statistical significance using a one-way ANOVA with Dunn's multiple comparison test. A p-value<0.05 was considered significant. Any other relevant statistical tests are noted in the appropriate figure legend.

ACKNOWLEDGEMENTS

We would like to thank staff at the Biological Imaging Facility, Mark Wainwright Analytical Centre, UNSW Sydney for technical assistance and Dr Daniel Brown, Curtin University for helpful discussions. This work was funded, in part, by an Australian Postgraduate Award to AR and National Health and Medical Research Council of Australia grants APP1101078 and APP1156944 to ND.

AUTHOR CONTRIBUTIONS

BJC developed the concept of the study. AR, SF, VL and BJC conducted experiments, data analysis and interpretation. BJC, AR and SF wrote the manuscript. KAR and NDG contributed to the manuscript through discussion, data interpretation and experimental design. All authors reviewed the manuscript.

REFERENCES

1 Azaripour, A. *et al.* A survey of clearing techniques for 3D imaging of tissues with special reference to connective tissue. *Prog Histochem Cytochem.* **51**, 9-23. doi: 10.1016/j.proghi.2016.1004.1001. Epub 2016 Apr 1014. (2016).

2 Richardson, A. *et al.* Keratin-14-positive precursor cells spawn a population of migratory corneal epithelia that maintain tissue mass throughout life. *Stem cell reports* **9**, 1081-1096, doi:10.1016/j.stemcr.2017.08.015 (2017).

3 Chung, K. & Deisseroth, K. CLARITY for mapping the nervous system. *Nat Methods.* **10**, 508-513. doi: 510.1038/nmeth.2481. (2013).

4 Chung, K. *et al.* Structural and molecular interrogation of intact biological systems. *Nature.* **497**, 332-337. doi: 310.1038/nature12107. Epub 12013 Apr 12110. (2013).

5 Susaki, E. A. *et al.* Whole-brain imaging with single-cell resolution using chemical cocktails and computational analysis. *Cell.* **157**, 726-739. doi: 710.1016/j.cell.2014.1003.1042. Epub 2014 Apr 1017. (2014).

6 Susaki, E. A. *et al.* Advanced CUBIC protocols for whole-brain and whole-body clearing and imaging. *Nat Protoc* **10**, 1709-1727, doi:10.1038/nprot.2015.085 (2015).

7 Susaki, Etsuo A. & Ueda, Hiroki R. Whole-body and Whole-Organ Clearing and Imaging Techniques with Single-Cell Resolution: Toward Organism-Level Systems Biology in Mammals. *Cell Chemical Biology* **23**, 137-157, doi:https://doi.org/10.1016/j.chembiol.2015.11.009 (2016).

8 Aoyagi, Y., Kawakami, R., Osanai, H., Hibi, T. & Nemoto, T. A rapid optical clearing protocol using 2,2'-thiodiethanol for microscopic observation of fixed mouse brain. *PLoS One.* **10**, e0116280. doi: 0116210.0111371/journal.pone.0116280. eCollection 0112015. (2015).

9 Ke, M. T., Fujimoto, S. & Imai, T. SeeDB: a simple and morphology-preserving optical clearing agent for neuronal circuit reconstruction. *Nat Neurosci.* **16**, 1154-1161. doi: 1110.1038/nn.3447. Epub 2013 Jun 1123. (2013).

10 Hama, H. *et al.* ScaleS: an optical clearing palette for biological imaging. *Nat Neurosci.* **18**, 1518-1529. doi: 1510.1038/nn.4107. Epub 2015 Sep 1514. (2015).

11 Williams, M. P. I. *et al.* A Novel Optical Tissue Clearing Protocol for Mouse Skeletal Muscle to Visualize Endplates in Their Tissue Context. *Front Cell Neurosci.* **13:49.**, 10.3389/fncel.2019.00049. eCollection 02019. (2019).

12 Becker, K., Jahrling, N., Saghafi, S., Weiler, R. & Dodt, H. U. Chemical clearing and dehydration of GFP expressing mouse brains. *PLoS One* **7**, e33916. doi: 33910.31371/journal.pone.0033916. Epub 0032012 Mar 0033930. (2012).

13 Erturk, A. *et al.* Three-dimensional imaging of solvent-cleared organs using 3DISCO. *Nat Protoc.* **7**, 1983-1995. doi: 1910.1038/nprot.2012.1119. Epub 2012 Oct 1911. (2012).

14 Pan, C., Cai, R., Quacquarelli, F. P., Gasemigharagoz, A. & Erturk, A. Whole organ and organism tissue clearing by uDISCO. (2016).

15 Jing, D. *et al.* Tissue clearing of both hard and soft tissue organs with the PEGASOS method. *Cell Research* **28**, 803-818, doi:10.1038/s41422-018-0049-z (2018).

16 Power, R. M. & Huisken, J. A guide to light-sheet fluorescence microscopy for multiscale imaging. *Nat Methods.* **14**, 360-373. doi: 310.1038/nmeth.4224. (2017).

17 Nojima, S. *et al.* CUBIC pathology: three-dimensional imaging for pathological diagnosis. *Scientific reports* **7**, 9269, doi:10.1038/s41598-017-09117-0 (2017).

18 Murakami, T. C. *et al.* A three-dimensional single-cell-resolution whole-brain atlas using CUBIC-X expansion microscopy and tissue clearing. *Nat Neurosci.* **21**, 625-637. doi: 610.1038/s41593-41018-40109-41591. Epub 42018 Mar 41595. (2018).

19 Chen, F., Tillberg, P. W. & Boyden, E. S. Optical imaging. Expansion microscopy. *Science.* **347**, 543-548. doi: 510.1126/science.1260088. Epub 1262015 Jan 1260015. (2015).

20 Cai, R. *et al.* Panoptic vDISCO imaging reveals neuronal connectivity, remote trauma effects and meningeal vessels in intact transparent mice. *bioRxiv* (2018).

21 Cai, R. *et al.* Panoptic imaging of transparent mice reveals whole-body neuronal projections and skull-meninges connections. *Nat Neurosci.* **22**, 317-327. doi: 310.1038/s41593-41018-40301-41593. Epub 42018 Dec 41531. (2019).

22 Pan, C. *et al.* Shrinkage-mediated imaging of entire organs and organisms using uDISCO. *Nat Methods.* **13**, 859-867. doi: 810.1038/nmeth.3964. Epub 2016 Aug 1022. (2016).

23 Park, Y. G. *et al.* Protection of tissue physicochemical properties using polyfunctional crosslinkers. *Nat Biotechnol* **17** (2018).

24 Rioboo, R. J. J., Desco, M. & Gomez-Gaviro, M. V. Impact of optical tissue clearing on the Brillouin signal from biological tissue samples. *Biomed Opt Express.* **10**, 2674-2683. doi: 2610.1364/BOE.2610.002674. eCollection 002019 Jun 002671. (2019).

25 Fretaud, M. *et al.* High-resolution 3D imaging of whole organ after clearing: taking a new look at the zebrafish testis. *Scientific reports* **7**, 43012, doi:10.1038/srep43012 (2017).

26 Becker, K. *et al.* Reduction of photo bleaching and long term archiving of chemically cleared GFP-expressing mouse brains. *PLoS One.* **9**, e114149. doi: 114110.111371/journal.pone.0114149. eCollection 0112014. (2014).

27 Zhou, C. *et al.* High water content hydrogel with super high refractive index. *Macromol Biosci* **13**, 1485-1491, doi:10.1002/mabi.201300191 (2013).

28 Murray, E. *et al.* Simple, Scalable Proteomic Imaging for High-Dimensional Profiling of Intact Systems. *Cell* **163**, 1500-1514, doi:10.1016/j.cell.2015.11.025 (2015).

29 Ahmed, E. M. Hydrogel: Preparation, characterization, and applications: A review. *J Adv Res.* **6**, 105-121. doi: 110.1016/j.jare.2013.1007.1006. Epub 2013 Jul 1018. (2015).

30 Kopecek, J. Hydrogels from Soft Contact Lenses and Implants to Self-Assembled Nanomaterials. *J Polym Sci A Polym Chem.* **47**, 5929-5946. doi: 5910.1002/pola.23607. (2009).

31 Khan, S., Ullah, A., Ullah, K. & Rehman, N.-u. Insight into hydrogels. *Designed Monomers and Polymers* **19**, 456-478, doi:10.1080/15685551.2016.1169380 (2016).

32 Hillman, E. M. C., Voleti, V., Li, W. & Yu, H. Light-Sheet Microscopy in Neuroscience. *Annu Rev Neurosci.* **42:295-313.**, 10.1146/annurev-neuro-070918-050357. (2019).

33 Di Giovanna, A. P. *et al.* Tailored Sample Mounting for Light-Sheet Fluorescence Microscopy of Clarified Specimens by Polydimethylsiloxane Casting. *Front Neuroanat* **13**, 35, doi:10.3389/fnana.2019.00035 (2019).

34 Belle, M. *et al.* Tridimensional Visualization and Analysis of Early Human Development. *Cell* **169**, 161-173 e112, doi:10.1016/j.cell.2017.03.008 (2017).

Figure Legends

Figure 1: Physical description of high RI hydrogels. The chemical structures of acrylamide (**A**), methacrylamide (**B**) and tri(ethlene glycol) dimethacrylate (**C**) are shown. Changes in hydrogel size following synthesis and immersion in PBS for 24 hours were measured (*n=8*) (**D**), together with the water content of high RI hydrogels (*n=8*) (**E**). Histograms (**D and E**) represent the mean ± sd and results were analysed by one-way ANOVA with Dunn's multiple comparison's test. *p<0.05, **p<0.01.

Figure 2: Antibody penetration, size changes in different media and high RI hydrogel motility over time. High RI hydrogels were assessed for their ability to influx (**A**) and efflux (**B**) IgG-FITC. Fluorescence intensity was quantified over 6 days. Histograms (**A and B**) represent mean (n=6/time point) fluorescence intensity ± SD. Hydrogels containing fluorescent microbeads were synthesized and serially imaged to determine the extent of gel motility (**C**). Images displayed are at t=0 and t=100 s, co-localization plot and scatter plot. Co-localization was analyzed using a Pearson's coefficient (r=0.737) and demonstrates a high degree of co-localization. Hydrogels were also analysed for volume changes in different refractive index matched solutions including distilled water (**D top row and E**), CUBIC-1 (**D second row and F**), CUBIC-2 (**D third row and G**) and RIMS (**D bottom row and H**). Histograms (**E-H**) represent mean (n=6/time point) hydrogel volume ± SD and is displayed as the percentage change from t=0 time point. data was analysed by one-way ANOVA and Dunn's multiple comparisons test. *p<0.05, **p<0.01, ***p<0.001, ****p<0.0001.

Figure 3: Light sheet fluorescence microscopy of CUBIC cleared mouse embryos. Representative images of an E14.5 embryo prior to (**A**) and following (**B**) clearing with the CUBIC protocol. To determine whether large biological samples could be embedded in high RI hydrogels prior to imaging, we stained and embedded mouse embryos at E12.5 (**C-E**) and

E14.5 (**F-I**) ages. Embryos were stained with lectin (**C and G**) and αSMA (**D and H**) and the images were merged (**E, F and I**). Various anatomical features were visible on both E12.5 and E14.5 embryos. Scale bars in all panels represent 1 mm.

Figure 4: LSFM of CUBIC cleared mouse heart and kidney. A volumetric representation of a mouse heart following staining with Hoechst 33324 nuclear stain demonstrating various anatomical features is shown in (**A**). The same portion of heart tissue as a maximum intensity projection displaying the same anatomical features is shown in (**B and C**). Mouse auricle stained with lectin (red) and αSMA (green) showing the blood supply of the tissue is shown in (**D-F**). Mouse kidneys were also stained with Hoechst 33342 (blue), αSMA (green) and lectin (red) (**G**), and clearly demonstrate the ureteric artery on the outside of the capsule. When stained with lectin, individual Loops of Henle were visible within the cortex of the kidney (**H closed arrows**) together with acuate arteries and venules (**H open arrows**). A volumetric representation of the vasculature of the murine kidney stained with lectin (red) and αSMA (green) is shown in (**I**).

Figure 1

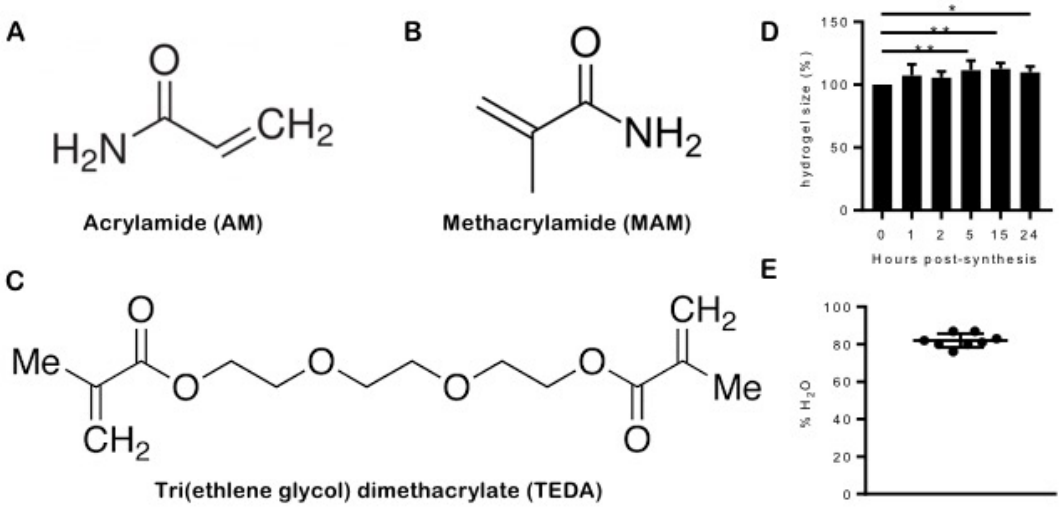

Figure 2

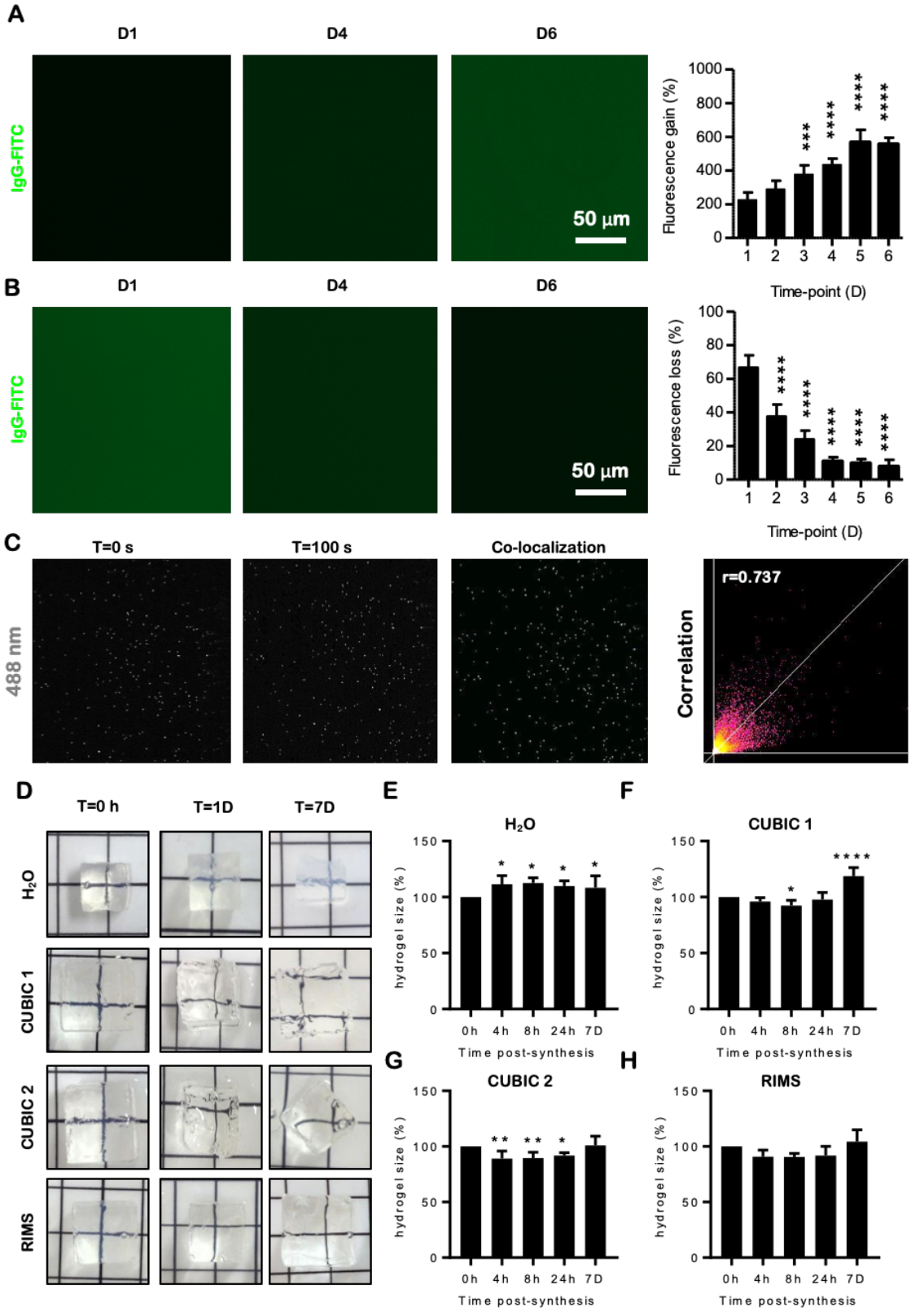

Figure 3

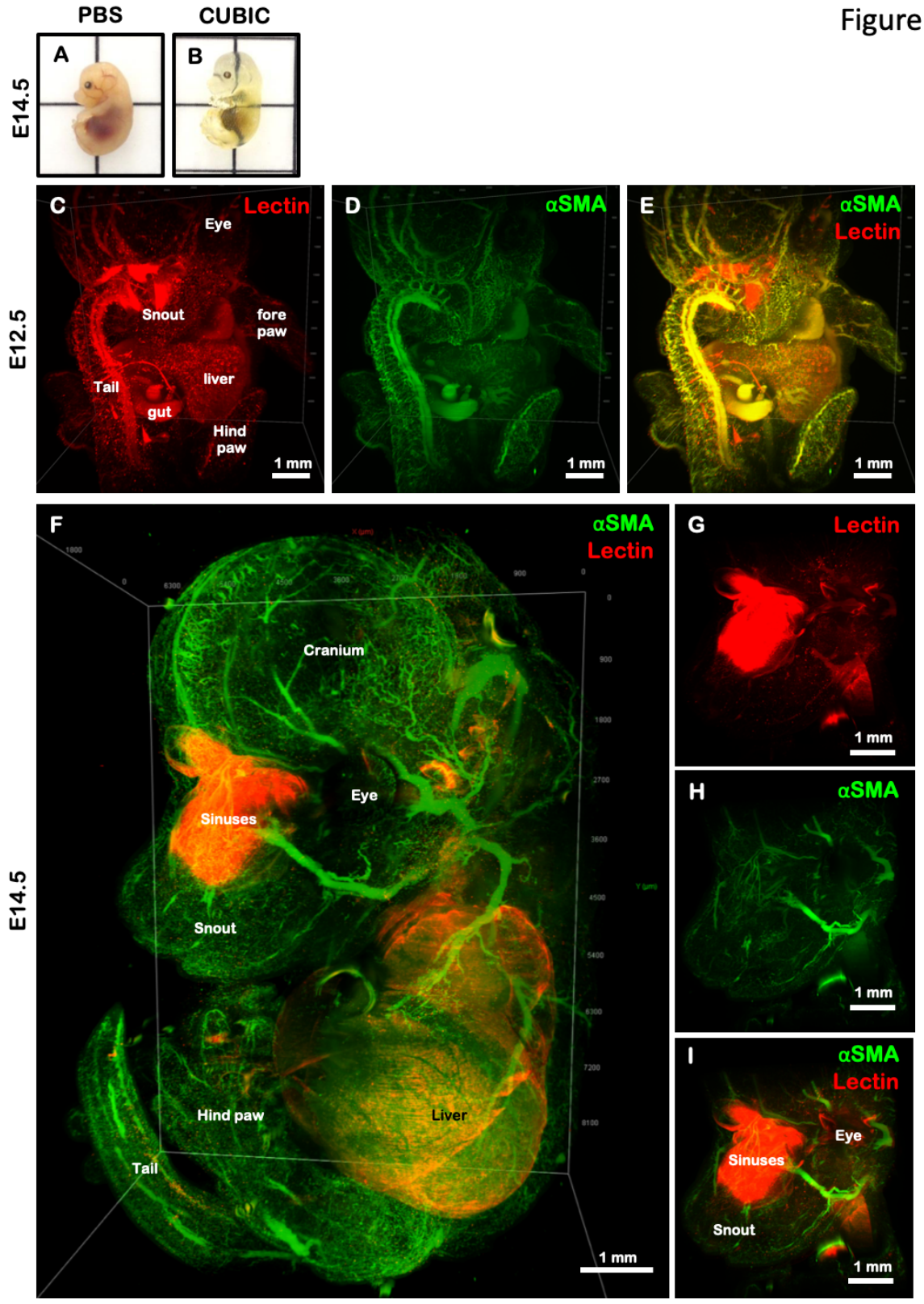

Figure 4

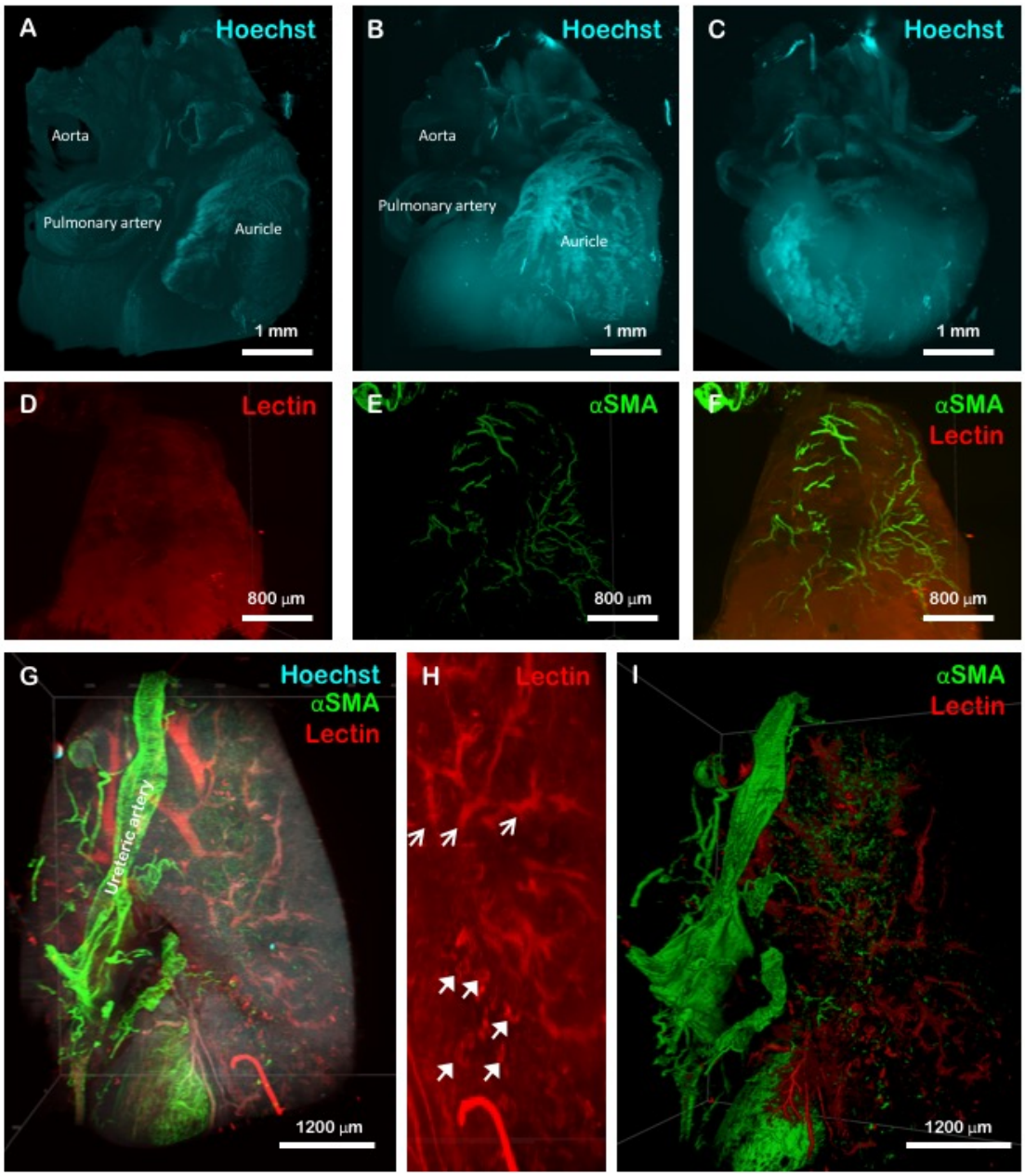

Supplementary Movie S1: Light sheet fluorescence microscopy of CUBIC cleared E14.5 mouse embryo.